Multislip-enabled morphing of all-inorganic perovskites

Xiaocui Li[1,2,3,6], You Meng[2,6], Wanpeng Li[2,3,6], Jun Zhang[1], Chaoqun Dang[4], Heyi Wang[1], Shih-Wei Hung[2,3], Rong Fan[1], Fu-Rong Chen[2,3]*, Shijun Zhao[1]*, Johnny C. Ho[2]*, Yang Lu[1,5]*

[1]Department of Mechanical Engineering, City University of Hong Kong, Kowloon, Hong Kong SAR, China

[2]Department of Materials Science and Engineering, City University of Hong Kong, Kowloon, Hong Kong SAR, China

[3]Time-resolved Aberration Corrected Environmental Electron Microscope Unit, City University of Hong Kong, Kowloon, Hong Kong SAR, China

[4]Center for X-mechanics, ZJU-Hangzhou Global Scientific and Technological Innovation Center, Zhejiang University, Hangzhou, China

[5]Department of Mechanical Engineering, The University of Hong Kong, Pokfulam, Hong Kong SAR, China

[6]These authors contributed equally: Xiaocui Li, You Meng, Wanpeng Li.

*Corresponding authors' Email addresses: frchen@cityu.edu.hk (F.-R.C); shijzhao@cityu.edu.hk (S.Z); johnnyho@cityu.edu.hk (J.C.H); ylu1@hku.hk (Y.L.)

All-inorganic lead halide perovskites ($CsPbX_3$, X=Cl, Br, I) are becoming increasingly important for energy conversion and optoelectronics because of their outstanding performance and enhanced environmental stability. Morphing perovskites into specific shapes/geometries without damaging their intrinsic functional properties is attractive for their device design and manufacturing. However, inorganic semiconductors are often intrinsically brittle at room temperature, except for some recently reported layered/van der Waals (vdW) semiconductors. Here, by *in situ* compression, we demonstrate that single-crystalline $CsPbX_3$ micropillars can be substantially morphed into distinct shapes (cubic, L- and Z-shape, rectangular arch, etc.) without localized cleavage/cracks. Such exceptional plasticity is enabled by successive slips of partial dislocations on multiple {110}<$1\bar{1}0$> systems, as evidenced by atomic resolution transmission electron microscopy (TEM) and first-principles and atomistic simulations. With devices demonstrated with unchanged optoelectronic performance and bandgap, our results suggest $CsPbX_3$ perovskites, as a potential class of deformable inorganic semiconductors, would have profound implications for the manufacture of advanced optoelectronics and energy systems.

Semiconductor materials with substantial room-temperature plastic deformability to adapt to desirable shapes without losing targeted electronic performance are promising in developing deformable electronics. The ability to be shapable and mechanically adaptable can ensure excellent processability and high conformability with other interfaces during device fabrication, as well as avoid brittle failure in practical utilization. The intrinsic softness and high deformability of organic semiconductors have rendered their applications in stretchable/deformable electronics[1]. However, the necessary molecular characteristics (such as high crystallinity) for desired charge

transport could embrittle them[2]. On the other hand, inorganic semiconductors usually have higher carrier mobility and much better electrical performance than organic semiconductors[3], but they are often brittle under ambient condition due to their directional covalent bonds or strong electrostatic interactions among ionic species[4]. When their dimensions/sizes reduced to micro/nanoscale, in addition to significantly enhanced elasticity[5-8], a certain amount of intrinsic plasticity can be achieved at room temperature[9-12]. Nonetheless, substantial plastic deforming and shaping remains unattainable for most bulk inorganic semiconductors, except for a few single crystal oxides with high concentration of oxygen vacancies and pre-existing dislocations[13-17] and ZnS single crystals deformed in darkness[18], as well as recently reported bulk layered/vdW semiconductors with extraordinary, metal-like room-temperature plasticity[19-21] thanks to their weak interlayer bonding and easy gliding. Other than that, plastic forming and morphing inorganic semiconductors into various shapes/geometries is still extremely attractive but uncommon, and to pursue large room-temperature ductility in inorganic semiconductors remains a holy grail for fabricating complicated devices and deformable electronics.

Here, we report that vapor-liquid-solid (VLS)-grown single-crystalline pillars of all-inorganic $CsPbX_3$ perovskites[22] can have unusual intrinsic plastic deformability under ambient condition: unprecedented geometry/shape morphing can be thus achieved *in situ* through continuous mechanical compression, without affecting their optoelectronic performance and electronic band structures. By using atomic resolution TEM analysis as well as first-principles and atomistic simulations, the successively and continuously activated partial dislocations on multiple low-energy-barrier $\{110\}\langle 1\bar{1}0\rangle$ slip systems (multislip) were verified to enable the observed substantial plasticity, with the strong Pb-X bonds maintaining crystal structure integrity and prevent

cracks/cleavage. Such unprecedented plasticity and morphing can be consistently achieved in single crystalline pillar samples with various dimensions (diameter and length up to ~2 μm and 10 μm, respectively) and aspect ratio (~1.7-14), while the corresponding compression strains that are easily accommodated by multislip can be well above ~60-70%. The present result, together with the above-mentioned outstanding optoelectronic and energy conversion performance[23,24], render $CsPbX_3$ perovskites as a group of promising ductile semiconductors for advanced deformable electronics and optoelectronics.

We first synthesized single-crystalline $CsPbX_3$ pillars with diameter/width ~0.4 to 2 μm and length ~3 to 10 μm via the VLS method[25]. Figure 1a shows the bright-field TEM image of a typical $CsPbBr_3$ pillar. The inset selected-area electron diffraction (SAED) pattern demonstrates the single-crystallinity and refers to an orthorhombic crystal structure[22]. By convention, the "pseudocubic" $CsPbX_3$ perovskites are indexed by cubic structure (Supplementary Fig. 1) to simplify the deformation analysis[26]. Fig. 1b shows an atomic resolution high angle annular dark field scanning transmission electron microscopy (HAADF-STEM) image processed by average background subtraction filter (ABSF)[27]. The atomic columns were identified according to contrast intensities and atomic number of each element, and a unit cell was superimposed to guide the view. The $CsPbX_3$ single crystalline pillars have near squared cross-sections (Fig. 1c and Supplementary Fig. 2), the corresponding chemical composition was examined by energy-dispersive X-ray spectroscopy (Supplementary Fig. 3). Quantitative *in situ* compressive experiments were then conducted inside a scanning electron microscope (SEM) by using a flat punch diamond indenter (Fig. 1d) to apply load and deform the $CsPbX_3$ single crystals (Fig. 1e).

Morphing can be actually well achieved in the family of single-crystalline $CsPbX_3$ perovskites. Figures 1f-k demonstrate various examples extracted from Supplementary Movie 1. The schematic diagrams of the original and morphed geometries were shown beside each sample. Fig. 1f demonstrates a "cubic" shape (front view) achieved in a $CsPbBr_3$ single crystal, the corresponding nominal compressive strain even reached ~75% (Supplementary Fig. 11). Interestingly, the crystal showed little lateral thickening since the deformation was accommodated by the alternating slips on a pair of conjugate slip systems. In the deformation of the $CsPbBr_3$ single crystal in Fig. 1g, slips were continuously activated on a single slip system, the crystal was facilely deformed into an upside-down "L"-shape. The $CsPbBr_3$ single crystal in Fig. 1h was firstly morphed into a distinct "Z"-shape, and eventually became almost flat rectangular spread on the substrate (Fig. 1h insert), like "falling dominoes", with an astonishing nominal compressive strain of ~83%. Fig. 1i further illustrates that a thick $CsPbBr_3$ single crystal with 1.85 μm width/thickness could also achieve multislip and was morphed into a "wine glass" shape. A "rectangular arch" geometry can be achieved in a $CsPbCl_3$ single crystal (Fig. 1j). The process of morphing a $CsPbI_3$ single crystalline pillar into "L"-shape is shown in Fig. 1k.

As shown in the experiments, such morphing was achieved by continuous slips operated on multiple slip systems (multislip) in $CsPbX_3$ single crystals. A paradigm of deformation in $CsPbX_3$ single crystals is presented in Figure 2. We extracted a series of SEM snapshots (Figs. 2a-h) from the *in situ* compressive video (Supplementary Movie 2) of a $CsPbBr_3$ single crystalline pillar, which was strikingly morphed into "L"-shape through "domino-like" successive slips on multiple systems, as highlighted by the colored illustrations below each snapshot. The events of SEM snapshots were indicated on the engineering stress-strain curve (Fig. 2i), which is composed of

intensive stress drops/strain bursts caused by continuous slips and followed by "elastic re-loading"[28]. These segments give an average yield stress of ~235±23 MPa and critical resolved shear stress (CRSS) of ~117±12 MPa, and their slopes give an average Young's modulus of 22.9±2.7 GPa, which is comparable with the theoretical value of the material[29]. The stress drops that fall nearly to zero indicate most of the dislocations can slip out of the single crystal with a relatively small sample volume, without accumulation[28]. All the slip activities were found in non-close-packed $\{110\}\langle 1\bar{1}0\rangle$ slip system (see Supplementary Note 2). Four specific equivalent $\{110\}\langle 1\bar{1}0\rangle$ slip systems exist under the present loading condition (Fig. 2j). For simplicity, hereinafter, they are named (and colored) as S_1 (blue), S_2 (orange), S_3 (red), and S_4 (green), respectively. Slips are activated on multiple systems in turn with the aid of pillar re-orientation. For example, when S_1 slip was in operation, lateral movement of the pillar was restricted by the indenter and substrate[4,30]. As a result, the pillar was forced to rotate (see the angle θ in Fig. 2b), and the resolved shear stress on each slip system changed, S_2 slip became geometrically preferred and was initiated as a consequence (Fig. 2c); details can be seen in Supplementary Notes 3-4. As proved by the yield stresses that showed no obvious increase, the alternate activation of multislip precludes dislocations from different slip systems to intersect with each other, thereby eliminating strain hardening and consequent formation of axial cracks, enabling the exceptional plasticity. The deformation in $CsPbI_3$ and $CsPbCl_3$ single crystals can be likewise achieved via multislip (Fig. 2k and Fig. 1j), suggesting the general exceptional ductility of the $CsPbX_3$ family. The activation of multislip was also validated by molecular dynamics (MD) simulation. The setup of a $CsPbBr_3$ single crystal for MD and its original stress state are shown in Fig. 2l. During compression, stress concentration (Fig. 2m) and slips

(Fig. 2n) occurred on multiple slip systems at the compressive strains of 9.3% and 10.3%, respectively, as indicated by the arrows.

To shed light on underlying plastic deformation mechanism of $CsPbX_3$ perovskites, atomic resolution HAADF-STEM characterization was conducted on a deformed $CsPbBr_3$ sample that carefully prepared by focus ion beam (FIB) cutting, as shown in Fig. 3a. The sample was found dislocation starved with most of the slip bands containing no residual dislocation (see Supplementary Fig. 8a). A very few residual dislocations were found on S_1 and S_2 slip systems (indicated by the squares in Fig. 3a). In HAADF-STEM image of S_1 dislocation (Fig. 3b), the dislocation cores were recognized by geometric phase analysis (GPA) (Supplementary Note 5) and marked by "⊥" symbols. Clearly a full dislocation dissociated into two partial dislocations $\boldsymbol{b_1}$ and $\boldsymbol{b_2}$ with Burgers vector of $\frac{1}{2}a<01\bar{1}>$, as depicted by the white dashed circuits. However, the partial pair was not collinearly distributed along the slip direction as expected[31]. S_2 dislocation showed a similar phenomenon with S_1 (Fig. 3c). To explain the dislocation configuration in $CsPbBr_3$, we calculated the generalized stacking fault energy (GSFE) profiles by first-principles density functional theory (DFT) calculations[32]. As shown in Fig. 3d, $\{110\}<1\bar{1}0>$ slip system exhibits the lowest energy barrier among the others, with the value of ~243 mJ/m^2. It is also noticed an energy minimum occurred at around the middle of the $\{110\}<1\bar{1}0>$ profile, suggesting a full dislocation tends to dissociate into two colinear partial dislocations. Besides, $\{001\}<010>$ has the lowest antiphase boundary (APB) energy of ~60 mJ/m^2, which induces the partial pairs to align along it. Therefore, we conclude the observed dislocation configuration is the result of colinear dissociation of a full dislocation during deformation and the migration of a partial along $\{001\}<010>$ ($\boldsymbol{b_2^0}$ **to** $\boldsymbol{b_2}$) when the sample was unloaded; details can be seen in Supplementary Note 5. Similar energy driven dissociation and adjustment of

dislocation have also been reported elsewhere[33].The smaller Burgers vector of partial dislocations would facilitate dislocation movement. As a comparison, there is no energy minimum in the GSFE profiles in rock salt (NaCl) structured ionic crystals[34], although they have the same active slip systems and comparable energy barriers, they are not as deformable as $CsPbX_3$ perovskites[10].

In addition to the continuous slips enabled by the low energy barrier, no cleavage generated during slip would be another key criterion for ductile materials. As depicted in HAADF-STEM images Figs. 3b-c and Supplementary Fig. 8, no increment in the interlayer spacing across the slip planes was observed in the deformed samples, which suggests no cleavage and high crystal cohesion upon morphing. We further compare the detailed energy cost of slippage on $\{110\}\langle 1\bar{1}0\rangle$ system based on DFT. Fig. 3e plots the variation of total energy as a function of interlayer spacing from the original equilibrium state. Here the six curves (marked by "dis_n") correspond to different gliding fractional displacements within the range from 0 to 0.5. The lowest energy was consistently obtained at the interlayer spacing variation of ~0 Å. The results demonstrated the excellent inherent crystal cohesion in $CsPbBr_3$. Compared with vdW semiconductors in which the interlayer separation varied widely during slipping[19], the crystal cohesion in $CsPbBr_3$ makes it less prone to cleavage. Besides, from the calculation, the slip energy E_S (energy barrier) and the cleavage energy E_C (defined by the difference between energy barrier and energy at an infinite interlayer distance) are determined as 0.021 eV/atom and 0.098 eV/atom, respectively. The relationship of $E_S \ll E_C$ further suggests our crystals can easily deform through slips while maintaining the structural integrity without cleaving.

To underpin the physical origin of the observed deformability and energy profiles, we further conducted detailed electronic and structural analyses. In the electron

localization functions (ELFs) of $CsPbBr_3$ (Figs. 3f-g), more electrons tend to populate between Br and Pb atoms than other pairs, leading to the stronger covalent bond of Br-Pb, which could maintain crystal cohesion and prevent the crystal from cleavage. The ELFs of $CsPbCl_3$ and $CsPbI_3$ also indicate electrons are localized between Cl-Pb and I-Pb bonds (Supplementary Fig. 10). Moreover, in the density of states (DOS) of bonding atoms (Fig. 3h), the peaks of Pb and Br overlap at -3.0 eV, while overlaps between Cs-Pb and Br-Cs are negligible. A linear model also confirms Br-Pb bonds play a key role in deformation (Supplementary Note 6). Therefore, we evaluated the variation of Br-Pb bond numbers in the faulted region when shearing along different slip systems (Fig. 3i). The results explain the trend of energy profiles in Fig. 3d well, e.g., the bond number changes least significantly along $\{110\}\langle 1\bar{1}0\rangle$, leading to the lowest shear resistance among others. Furthermore, we compared the strength within the $CsPbX_3$ family by projecting their crystal orbital Hamilton populations (COHPs) onto X-Pb bonds and integrating to the Fermi level (Fig. 3j). The bond strengths show a trend of Cl-Pb>Br-Pb>I-Pb, which is consistent not only with the experimentally measured yield stresses and Young's moduli in $CsPbX_3$, but also with the $\{110\}\langle 1\bar{1}0\rangle$ energy barriers, ~384 mJ/m^2 ($CsPbCl_3$), ~243mJ/m^2 ($CsPbBr_3$) and ~210 mJ/m^2 ($CsPbI_3$), see Supplementary Note 7. These sufficient low energy barriers compared with other perovskite materials (e.g., ~1230 mJ/m^2 in $SrTiO_3$)[31], together with the strong X-Pb bonds, have endowed $CsPbX_3$ continuous slips while maintaining crystal integration and cohesion. Exceptional plasticity can thus be consistently achieved in samples with dispersive diameter and aspect ratio, despite that the observations limited in micro-sized samples, giving an average slip-mediated strain of ~64%±8% (see supplementary Fig. 13).

We further demonstrated that this kind of plastic morphing can be applied in constructing patterned photodetector devices (Fig. 4a) with undegraded performance. Variform photodetectors were fabricated according to the geometries of morphed pillars (Figs. 4b-c). As expected, their photocurrent was comparable with that of the pristine pillars (Supplementary Fig. 14). We then measured the image sensing ability of photodetectors based on pristine and deformed pillars (see methods). Their two-dimensional photocurrent maps of a "peace dove" shaped hollowed mask exhibited almost the same pattern and intensity (Figs. 4d-e). More importantly, these two kinds of photodetectors followed the same power law relationship of $I(P) \sim P^{0.88}$, where I is photocurrent and P is incident light intensity (Fig. 4f). The transient photoresponse of pristine and deformed pillars was also measured under a chopping frequency of 500 Hz, both photodetectors showed rise time t_r of ~350 μs and fall time t_f of ~300 μs (Fig. 4g). The almost same optoelectronic performance in deformed pillars indicated unchanged electron-hole generation, recombination, and carrier-carrier interactions, which stemmed from the unchanged microstructure. To assess the impact of deformation on the electronic properties of $CsPbX_3$ single crystals, *in situ* cathodoluminescence (CL) characterization was conducted. Fig. 4h demonstrates SEM and CL images of an as-fabricated $CsPbBr_3$ pillar. The corresponding CL spectrum shows a typical emission peak at ~530 nm, which refers to intrinsic bandgap energy of ~2.34 eV[35]. After the pillar was compressed into "L"-shape by ~30% compressive strain (Fig. 4i), the local CL spectra obtained from three deformed regions consistently give a peak at ~530 nm, the value is almost the same as that before deformation. An additional example showing a similar result is shown in Supplementary Fig. 15. The unaffected optoelectronic performance and bandgap in morphed $CsPbX_3$ single crystals may also render potential applications in deformable devices.

Our results demonstrate that all-inorganic $CsPbX_3$ perovskite single crystals can be substantially deformed and facilely morphed into distinct geometries/shapes through the successive, "domino-like" multislip under ambient conditions, without damaging their crystalline integrity, lattice structure, and attractive optoelectronic properties. By comparing with the plastic deformation mechanisms of other ductile semiconductors, our finding suggests micro-sized ionic $CsPbX_3$ perovskites, as a class of intrinsic ductile inorganic semiconductors, would find enormous application potential for manufacturing next-generation deformable electronics, optoelectronics, and energy devices.

Acknowledgements

This work was supported by Hong Kong Research Grant Council (RGC) under Grant No. RFS2021-1S05 (Y.L.), 11200421 (S.Z) and CityU11306520 (J.C.H.), City University of Hong Kong under Grant No. 9610461 (Y.L.), and National Natural Science Foundation of China (NSFC)/RGC Joint Research Scheme under Grant No. N_HKU159/22 (Y.L.).

Author Contributions

Y.L. and X.L. conceived the research; Y.L., S.Z., F.-R.C and J.C.H. supervised the research; X.L. performed the experiments; Y.M. synthesized the samples and investigated the optoelectronic devices; W.L. fabricated FIB samples and performed part of analyses; S.Z. and J. Z. performed the simulations and calculations; C.D., H.W., S.-W.H. and R.F. performed part of analysis; X.L., Y.M., W.L., F.-R.C., S.Z., J.C.H. and Y.L. analyzed the data and wrote the initial manuscript; All authors contributed to the final manuscript and approved the submission.

Competing Interests

The authors declare that they have no competing interests.

Figure captions

Fig. 1. Material characterization, *in situ* experiment, and morphing of $CsPbX_3$ single crystals into various geometries. a, Bright-field transmission electron microscopy (BF-TEM) image of a $CsPbBr_3$ single crystalline pillar, inset is the selected-area electron diffraction (SAED) pattern of it. **b**, Average background subtraction filtered (ABSF) high angle annular dark field scanning transmission electron microscopy (HAADF-STEM) image of $CsPbBr_3$, the elements were identified by the superimposed unit cell on it. **c,** A top view of a $CsPbBr_3$ single crystalline pillar, showing squared cross-section. **d-e** Scanning electron microscopy (SEM) images of a flat punch diamond indenter (**d**) and a $CsPbBr_3$ pillar (**e)** grown vertically on the substrate, to illustrate the compression morphing process. **f-k,** Snapshots of *in situ* morphing of various $CsPbBr_3$ single crystals with different sizes (**f-i**), a $CsPbCl_3$ single crystal (**j**) and a $CsPbI_3$ single crystal (**k**). The schematic diagrams of their original and deformed geometries were shown beside the SEM snapshots.

Fig. 2. Morphing of a $CsPbBr_3$ single crystal through successive multislip. a-h, SEM snapshots of *in situ* compression process. Cartoons that reproducing the pillar geometries in each snapshot were given below. Different colors were used to highlight the activation of multiple slip systems. **i,** Engineering stress-strain curve colored according to the operated slip systems. The events in (**a-h**) were indicated on it. **j,** A unit cell of $CsPbBr_3$ that shows four equivalent $\{110\}\langle 1\bar{1}0\rangle$ slip systems under current loading geometry, named (and colored) as S_1 (blue), S_2 (orange), S_3 (red) and S_4 (green), respectively. **k,** A deformed $CsPbI_3$ single crystal, showing multislip. **l,** The setup of a

$CsPbBr_3$ single crystal for molecular dynamics (MD) simulation, and its stress state before compression. **m-n,** The stress states of the crystal at 9.3% and 10.3% compression strain, respectively. Projection views along [100] and [010] were provided, and the multiple slips were indicated by the colored arrows.

Fig. 3 Deformation mechanism and the origin of the exceptional plasticity in $CsPbX_3$ perovskites. a, A thin slice sample fabricated from a deformed $CsPbBr_3$ single crystal. **b-c**, HAADF-STEM images taken from "S_1" and "S_2" indicated in (**a**), showing the dislocation configuration. **d,** Generalized stacking fault energy (GSFE) profiles of several low-index slip systems in $CsPbBr_3$, suggesting that $\{110\}<1\bar{1}0>$ has the lowest energy barrier. **e,** The energy change as a function of interlayer spacing relative to the original equilibrium state. Curves correspond to six different fractional displacements (range from 0 to 0.5) were provided and marked by "dis_n". **f-g,** The electron localization functions (ELFs) on $[011]_{pc}$ projection and $[100]_{pc}$ projection in $CsPbBr_3$. **h,** Density of states (DOS) of bonding atoms in $CsPbBr_3$. **i.** The variation of Br-Pb bond numbers when slip along different systems. **j,** Projected crystal orbital Hamilton populations (pCOHP) of X-Pb bonds in $CsPbX_3$. The integration of pCOHP from negative infinity to the Fermi level is denoted in parentheses.

Fig. 4. Application of the morphed $CsPbX_3$ crystals in constructing patterned photodetector devices and optoelectronic performance characterization. a, The basic configuration of photodetector. Inset shows a photodetector based on a pristine pillar. **b-c,** Variform photodetectors fabricated with morphed pillars that have various geometries. **d-e,** The two-dimensional photocurrent maps of a "peace dove" shaped hollowed mask of photodetectors based on pristine pillar and deformed pillar. **f,** The photocurrent-light intensity (*I-P*) relationship, showing a power-law of $I(P) \sim P^{0.88}$. **g,** Transient photoresponses of pristine and deformed pillar under a chopping frequency

of 500 Hz. **h,** SEM and cathodoluminescence (CL) images of an as-fabricated $CsPbBr_3$ pillar, and the corresponding CL spectrum showing an intrinsic emission peak at ~ 530 nm. **i,** SEM and CL images of the same pillar after being compressed to 30% strain. The CL spectra from three different deformed regions showed almost unchanged emission peaks.

References

1 Oh, J. Y. *et al.* Intrinsically stretchable and healable semiconducting polymer for organic transistors. *Nature* **539**, 411-415, (2016).

2 Root, S. E., Savagatrup, S., Printz, A. D., Rodriquez, D. & Lipomi, D. J. Mechanical properties of organic semiconductors for stretchable, highly flexible, and mechanically robust electronics. *Chem. Rev.* **117**, 6467-6499, (2017).

3 Chen, H. *et al.* Room-temperature plastic inorganic semiconductors for flexible and deformable electronics. *InfoMat* **3**, 22-35, (2021).

4 Hertzberg, R. W., Vinci, R. P. & Hertzberg, J. L. *Deformation and Fracture Mechanics of Engineering Materials*. (John Wiley & Sons, 2020).

5 Zhang, H. *et al.* Approaching the ideal elastic strain limit in silicon nanowires. *Sci. Adv.* **2**, e1501382, (2016).

6 Dang, C. *et al.* Achieving large uniform tensile elasticity in microfabricated diamond. *Science* **371**, 76-78, (2021).

7 Wei, B. *et al.* Size-dependent bandgap modulation of ZnO nanowires by tensile strain. *Nano Lett.* **12**, 4595-4599, (2012).

8 Li, X. *et al.* High elasticity of $CsPbBr_3$ perovskite nanowires for flexible electronics. *Nano Res.* **14**, 4033-4037, (2021).

9 Chen, M. *et al.* Achieving micron-scale plasticity and theoretical strength in Silicon. *Nat. Commun.* **11**, 2681, (2020).

10 Zou, Y. & Spolenak, R. Size-dependent plasticity in micron- and submicron-sized ionic crystals. *Philos. Mag. Lett.* **93**, 431-438, (2013).

11 Fujikane, M., Nagao, S., Chrobak, D., Yokogawa, T. & Nowak, R. Room-temperature plasticity of a nanosized GaN crystal. *Nano Lett.* **21**, 6425-6431, (2021).

12 Mathews, N. G., Saxena, A. K., Kirchlechner, C., Dehm, G. & Jaya, B. N. Effect of size and domain orientation on strength of Barium Titanate. *Scr. Mater.* **182**, 68-73, (2020).

13 Liu, Y. *et al.* Giant room temperature compression and bending in ferroelectric oxide pillars. *Nat. Commun.* **13**, 335, (2022).

14 Yang, K. H., Ho, N. J. & Lu, H. Y. Plastic deformation of <001> single-crystal $SrTiO_3$ by compression at room temperature. *J. Am. Ceram. Soc.* **94**, 3104-3111, (2011).

15 Stich, S. *et al.* Room-temperature dislocation plasticity in $SrTiO_3$ tuned by defect chemistry. *J. Am. Ceram. Soc.* **105**, 1318-1329, (2022).

16 Li, Y. *et al.* Theoretical insights into the Peierls plasticity in $SrTiO_3$ ceramics via dislocation remodelling. *Nat. Commun.* **13**, 6925, (2022).

17 Gumbsch, P., Taeri-Baghbadrani, S., Brunner, D., Sigle, W. & Rühle, M. Plasticity and an Inverse Brittle-to-Ductile Transition in Strontium Titanate. *Phys. Rev. Lett.* **87**, 085505, (2001).

18 Oshima, Y., Nakamura, A. & Matsunaga, K. Extraordinary plasticity of an inorganic semiconductor in darkness. *Science* **360**, 772-774, (2018).
19 Shi, X. *et al.* Room-temperature ductile inorganic semiconductor. *Nat. Mater.* **17**, 421-426, (2018).
20 Wei, T.-R. *et al.* Exceptional plasticity in the bulk single-crystalline van der Waals semiconductor InSe. *Science* **369**, 542-545, (2020).
21 Wang, H. *et al.* Orientation-dependent large plasticity of single-crystalline gallium selenide. *Cell Rep. Phys. Sci.* **3**, 100816, (2022).
22 Zhang, J., Hodes, G., Jin, Z. & Liu, S. All-inorganic $CsPbX_3$ perovskite solar cells: progress and prospects. *Angew. Chem. Int. Ed.* **58**, 15596-15618, (2019).
23 Fu, Y. *et al.* Metal halide perovskite nanostructures for optoelectronic applications and the study of physical properties. *Nat. Rev. Mater.* **4**, 169-188, (2019).
24 Wang, Y. *et al.* Thermodynamically stabilized β-$CsPbI_3$-based perovskite solar cells with efficiencies >18%. *Science* **365**, 591-595, (2019).
25 Meng, Y. *et al.* Direct vapor-liquid-solid synthesis of all-inorganic perovskite nanowires for high-performance electronics and optoelectronics. *ACS Nano* **13**, 6060-6070, (2019).
26 Steele, J. A. *et al.* Thermal unequilibrium of strained black $CsPbI_3$ thin films. *Science* **365**, 679-684, (2019).
27 Kilaas, R. Optimal and near-optimal filters in high-resolution electron microscopy. *J. Microsc.* **190**, 45-51, (1998).
28 Greer, J. R., Oliver, W. C. & Nix, W. D. Size dependence of mechanical properties of gold at the micron scale in the absence of strain gradients. *Acta Mater.* **53**, 1821-1830, (2005).
29 Roknuzzaman, M., Ostrikov, K., Wang, H., Du, A. & Tesfamichael, T. Towards lead-free perovskite photovoltaics and optoelectronics by ab-initio simulations. *Scientific Reports* **7**, 14025, (2017).
30 Wang, Q., Wang, J., Li, J., Zhang, Z. & Mao, S. X. Consecutive crystallographic reorientations and superplasticity in body-centered cubic niobium nanowires. *Sci. Adv.* **4**, eaas8850, (2018).
31 Hirel, P., Marton, P., Mrovec, M. & Elsässer, C. Theoretical investigation of {110} generalized stacking faults and their relation to dislocation behavior in perovskite oxides. *Acta Mater.* **58**, 6072-6079, (2010).
32 Zhao, S., Stocks, G. M. & Zhang, Y. Stacking fault energies of face-centered cubic concentrated solid solution alloys. *Acta Mater.* **134**, 334-345, (2017).
33 Wu, Z. & Curtin, W. A. The origins of high hardening and low ductility in magnesium. *Nature* **526**, 62-67, (2015).
34 Nakamura, A. *et al.* First-principles calculations on slip system activation in the rock salt structure: electronic origin of ductility in silver chloride. *Philos. Mag.* **97**, 1281-1310, (2017).
35 Caicedo-Dávila, S. *et al.* Spatial phase distributions in solution-based and evaporated Cs–Pb–Br thin films. *J. Phys. Chem. C* **123**, 17666-17677, (2019).

Methods

Fabrication of $CsPbX_3$ (X=Cl, Br, I) single-crystalline pillars. The Vapor-Liquid-Solid (VLS) synthesis method was used for the fabrication of $CsPbX_3$ single-crystalline pillars[25]. To prepare the growth substrates, aqueous suspension of ~150-nm-diameter Sn nanoparticles (≥99 %, Aldrich™) in alcohol was drop-casted onto the thermally

grown SiO_2/Si substrates and then naturally dried. To obtain the $CsPbX_3$ source powder, CsX (99.9 %, Aldrich^{TM}) and PbX_2 (99.999 %, Aldrich^{TM}) powders with a molar ratio of 2:1 were mixed together and then annealed (at 460 °C for $CsPbCl_3$, 430 °C for $CsPbBr_3$ and 420 °C for $CsPbI_3$) for 30 min. In a two-zone CVD system, the $CsPbX_3$ source powder and growth substrates were placed at the high-temperature zone (470 °C for $CsPbCl_3$, 440 °C for $CsPbBr_3$ and 430 °C for $CsPbI_3$) and low-temperature zone (330 °C for $CsPbCl_3$, 300 °C for $CsPbBr_3$ and 290 °C for $CsPbI_3$), respectively. During the growth, the chamber pressure was set to 0.8 Torr, whereas the Ar gas with a flow speed of 80 sccm was used as a carrier gas. After the growth duration, $CsPbX_3$ pillars with various sizes were grown vertically on the growth substrates. Thin slices of deformed $CsPbBr_3$ pillars were prepared by focused ion beam (FIB, FEI Scios Dual Beam system) for atomic resolution TEM analysis.

Electron microscopy characterizations. The SEM images were taken by using a field-emission scanning electron microscope (FEI Quanta^{TM} 450 FE-SEM) that operated at 10 KV. The TEM characterizations were conducted by using a field-emission transmission electron microscope (JEOL^{TM} JEM-2100F FE-TEM) that operated at 200 KV. Elemental mapping was performed by the energy-dispersive X-ray spectroscopy (EDS) detector attached to the SEM and the detector attached to the TEM. Cathodoluminescence (CL) characterization was conducted by the Gatan Monarc^{TM} CL detector installed on the SEM. The high angle annular dark field scanning transmission electron microscopy (HAADF-STEM) was conducted on a spherical aberration corrected TEM JEOL^{TM} JEM-ARM300F2. To avoid the decomposition of beam sensitive $CsPbBr_3$ perovskites[36], a high accelerating voltage (300 KV) was used to suppress radiolysis (inelastic scattering that breaks the chemical bonds of the material)[37],

while a customized electrostatic dose modulator (EDM) was used to lower the electron dose rate down to 5% (~0.05 e/Å^2/s) for sample protection.

***in situ* Compression for morphing.** The *in situ* SEM compression experiments of $CsPbX_3$ pillars were based on a quantitative nanoindenter (Hysitron^{TM} PI85 SEM PicoIndenter)[5] in conjunction with the SEM. Firstly, a substrate with $CsPbX_3$ pillars grown vertically on it has been fixed on the stage. Then the relative position of pillars and flat punch diamond indenter was adjusted to ensure them in alignment. The *in situ* compression experiments were achieved by downwards movements of the diamond indenter which was controlled by the PI85 PicoIndenter. The loading was under displacement control mode with a constant loading velocity of 20 nm/s. The load-displacement data can be read from the high-resolution indenter, while the displacement of compression deformation can be further measured and calibrated based on *in situ* SEM images.

Photodetector device fabrication and characterization. To fabricate photodetectors, we pushed the pristine samples and deformed samples by a nanoindenter inside SEM, to let them lie onto the SiO_2/Si substrates. We then use FIB to coat 50 nm thick Pt electrodes on both ends of samples. The optoelectronic performance of the photodetectors was characterized by an Agilent 4155C semiconductor analyzer with a standard probe station. We used a laser with a wavelength of 450 nm to irradiate the photodetectors, while the incident light power was measured by a power meter (PM400, Thorlabs). To measure the image sensing ability of photodetectors, a “peace dove” shaped hollowed mask, which was controlled by a X-Y planar moving stage, was placed between the incident laser and photodetectors, while the photocurrent chopped by the moving mask was recorded in real time to generate two-dimensional photocurrent maps[38]. Transient photoresponses of pristine and deformed pillars were measured by a

home-built high-speed photoresponse measurement system, which composed of the light chopper (with a chopping frequency of 500 Hz), current amplifier, and digital oscilloscope.

Molecular dynamics (MD) simulation.

MD simulations were performed using the Large-scale atomic/molecular massively parallel simulation (LAMMPS) code[39]. The interatomic interactions among Cs-Pb-Br were described by the short-range repulsive part of the Buckingham type and a long-range part with Coulomb interactions. The potential parameters are from previous studies[40,41]. The Ewald summation method was used to account for the long-range nature of Coulomb forces. To simulate the compression of the crystal, we constructed supercells with a longer length along the z-direction, and the cross-section was in a square shape. The ratio of Lz/Lx(Ly) is 6. After equilibrium for 150 ps at 300 K, we applied compression by deforming the simulation box. During compression, the system was relaxed using the NVT ensemble with the Nosé-Hoover thermostat at 300 K[42]. The strain rate was 10^{-6}/fs.

Density functional theory (DFT) calculation. The calculations were performed using the Vienna ab initio Simulation Package based on the projector-augmented-wave method[43,44]. The generalized gradient approximation in the Perdew-Burke-Ernzerhof (PBE) form[45] was used to describe the exchange-correlation interactions. The energy cutoff was 350 eV. Supercells with different orientations were built to calculate the GSFE for different slip systems. At least 15 atomic layers were included in the model, with a 10 Å vacuum layer along the z direction. The k-points were sampled with a spacing of 0.2 $Å^{-1}$ in all cases. The upper half of the model was continuously shifted with respect to the lower half to simulate the shear process. The stacking fault energies

were calculated by the energy difference between the stacking fault structure and the perfect structure, scaled by the stacking fault area.

Data availability

The data supporting the findings of this study are available from the corresponding authors upon reasonable request.

Methods-only references

36 Zhou, Y., Sternlicht, H. & Padture, N. P. Transmission Electron Microscopy of Halide Perovskite Materials and Devices. *Joule* **3**, 641-661, (2019).

37 Egerton, R. F., Li, P. & Malac, M. Radiation damage in the TEM and SEM. *Micron* **35**, 399-409, (2004).

38 Wang, W. *et al.* Mixed-dimensional anti-ambipolar phototransistors based on 1D GaAsSb/2D MoS_2 heterojunctions. *ACS Nano* **16**, 11036-11048, (2022).

39 Plimpton, S. Fast parallel algorithms for short-range molecular dynamics. *J. Comput. Phys.* **117**, 1-19, (1995).

40 Lai, M. *et al.* Intrinsic anion diffusivity in lead halide perovskites is facilitated by a soft lattice. *Proc. Natl. Acad. Sci.* **115**, 11929-11934, (2018).

41 Mattoni, A., Filippetti, A. & Caddeo, C. Modeling hybrid perovskites by molecular dynamics. *J. Phys.: Condens. Matter* **29**, 043001, (2016).

42 Nosé, S. A unified formulation of the constant temperature molecular dynamics methods. *J. Chem. Phys.* **81**, 511-519, (1984).

43 Blöchl, P. E. Projector augmented-wave method. *Phys. Rev. B* **50**, 17953, (1994).

44 Kresse, G. & Hafner, J. Ab initio molecular dynamics for liquid metals. *Phys. Rev. B* **47**, 558, (1993).

45 Perdew, J. P., Burke, K. & Ernzerhof, M. Generalized gradient approximation made simple. *Phys. Rev. Lett.* **77**, 3865, (1996).

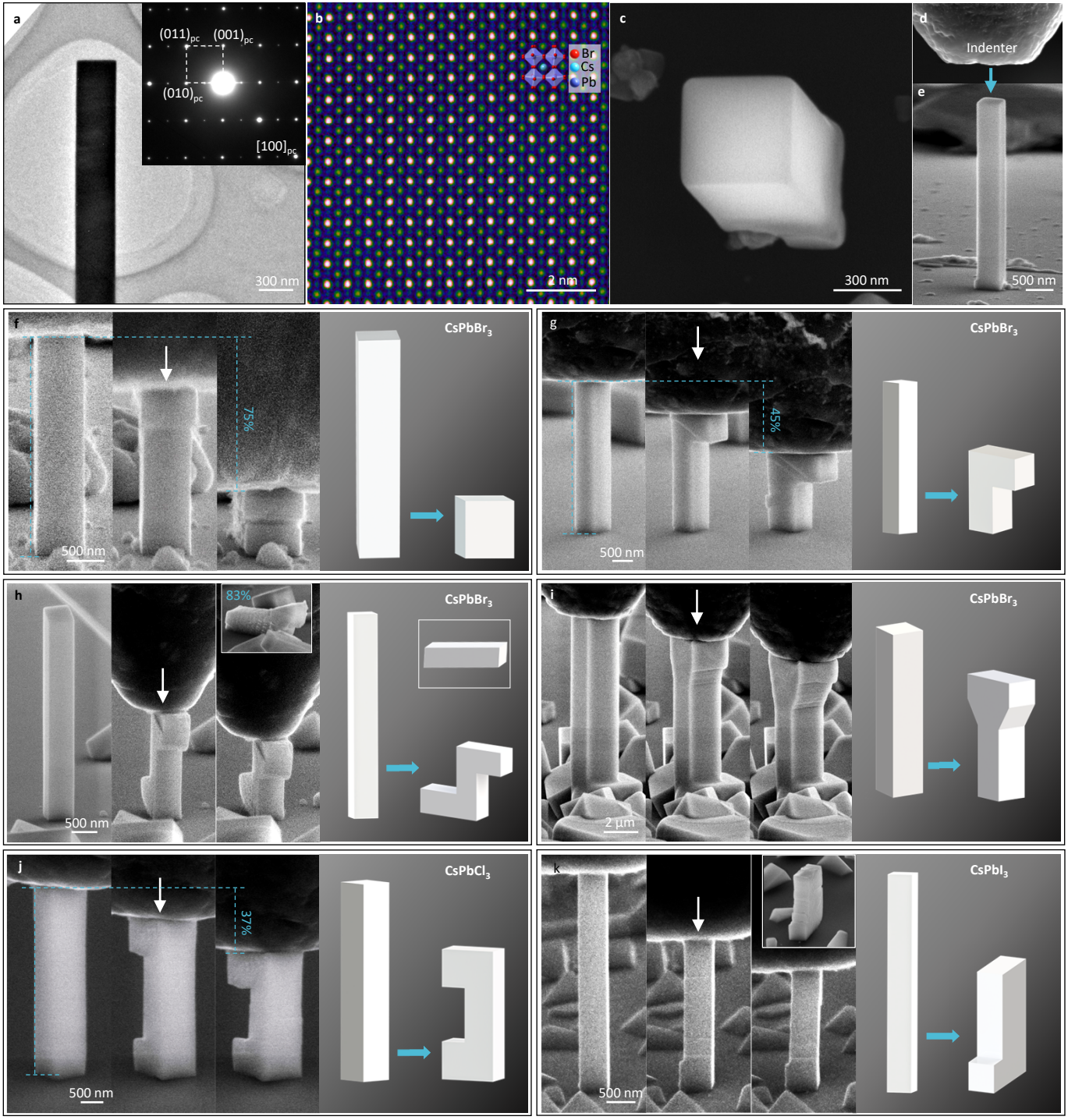
a
(011)pc
(001)pc
(010)pc
[100]pc
300 nm
b
Br
Cs
Pb
2 nm
c
300 nm
d
Indenter
e
500 nm
f
CsPbBr3
75%
500 nm
g
CsPbBr3
45%
500 nm
h
83%
CsPbBr3
500 nm
i
CsPbBr3
2 µm
j
CsPbCl3
37%
500 nm
k
CsPbI3
500 nm

Fig. 1

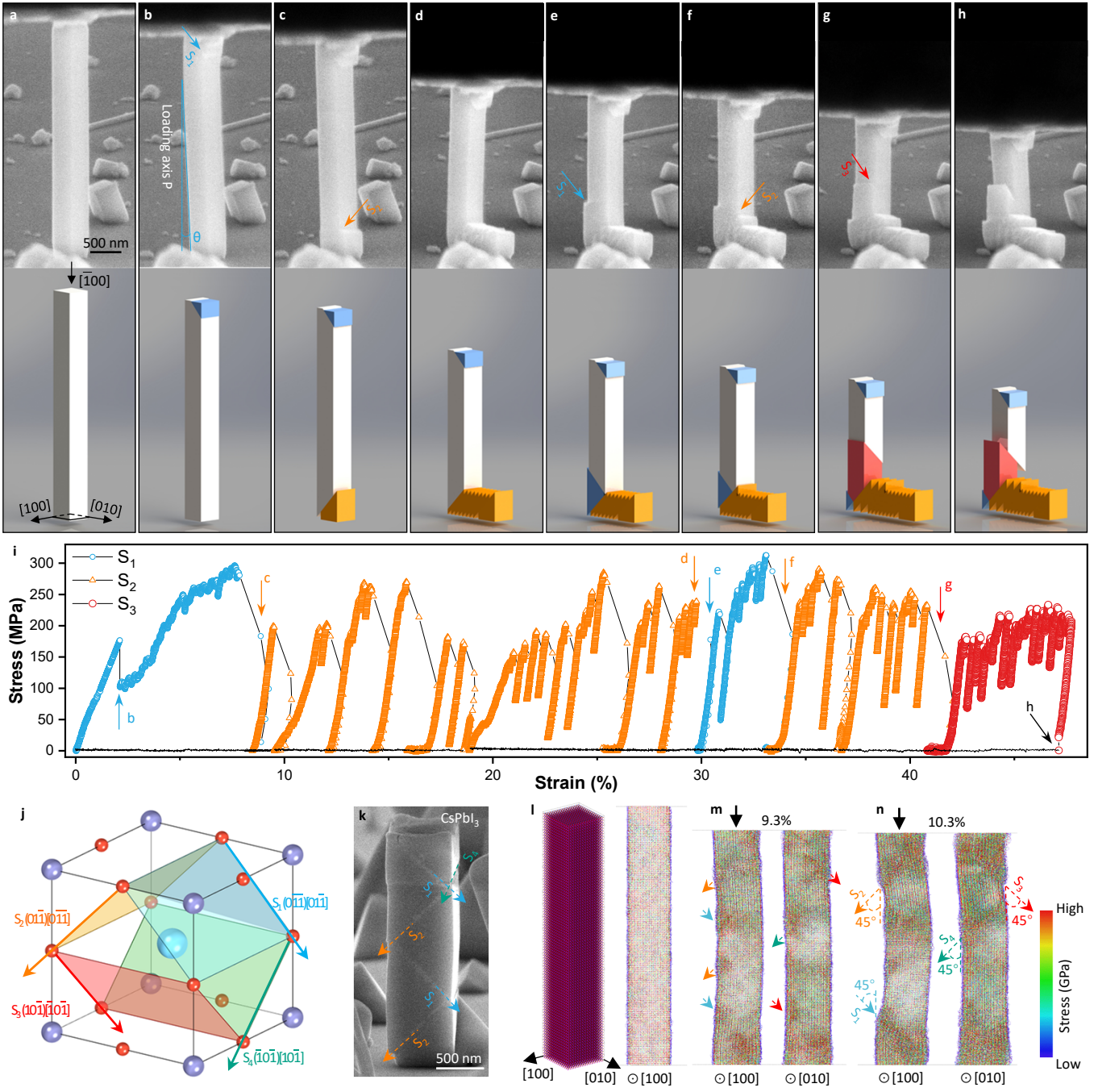
a
b
c
d
e
f
g
h
500 nm
[$\bar{1}$00]
Loading axis P
θ
[100]
[010]
i
Stress (MPa)
Strain (%)
S1
S2
S3
j
k
CsPbI3
500 nm
l
m
n
9.3%
10.3%
45°
High
Low
Stress (GPa)

Fig. 2

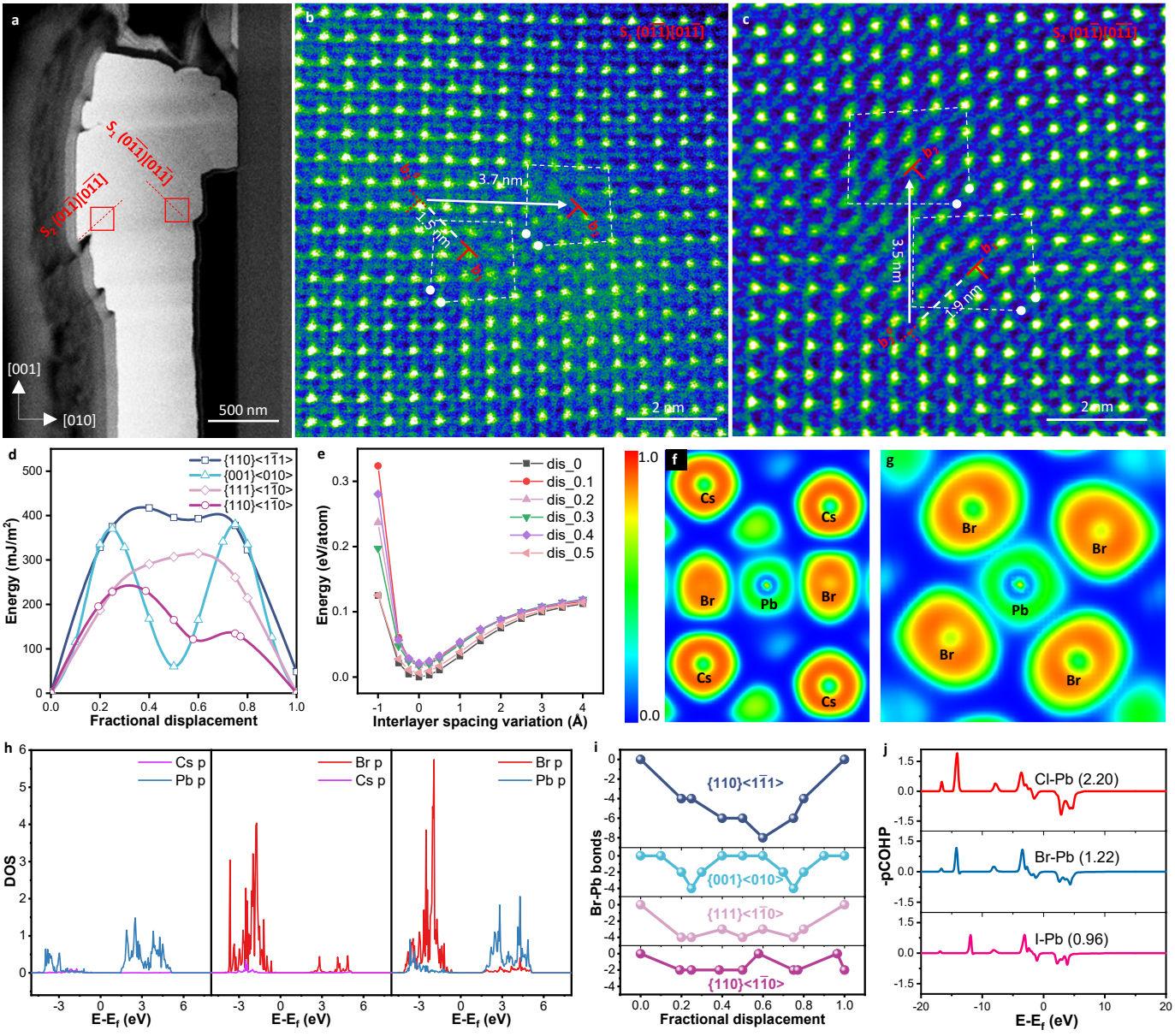
a
S1 (01$\bar{1}$)[011]
S2 (011)[01$\bar{1}$]
[001]
[010]
500 nm
b
S1 (01$\bar{1}$)[011]
3.7 nm
2 nm
c
S2 (011)[01$\bar{1}$]
3.5 nm
1.9 nm
2 nm
d
{110}<1$\bar{1}$1>
{001}<010>
{111}<1$\bar{1}$0>
{110}<1$\bar{1}$0>
Energy (mJ/m^2)
Fractional displacement
e
dis_0
dis_0.1
dis_0.2
dis_0.3
dis_0.4
dis_0.5
Energy (eV/atom)
Interlayer spacing variation (Å)
f
1.0
0.0
Cs
Br
Pb
g
Br
Pb
h
Cs p
Pb p
Br p
Cs p
Br p
Pb p
DOS
E-E$_f$ (eV)
i
{110}<1$\bar{1}$1>
{001}<010>
{111}<1$\bar{1}$0>
{110}<1$\bar{1}$0>
Br-Pb bonds
Fractional displacement
j
Cl-Pb (2.20)
Br-Pb (1.22)
I-Pb (0.96)
-pCOHP
E-E$_f$ (eV)

Fig. 3

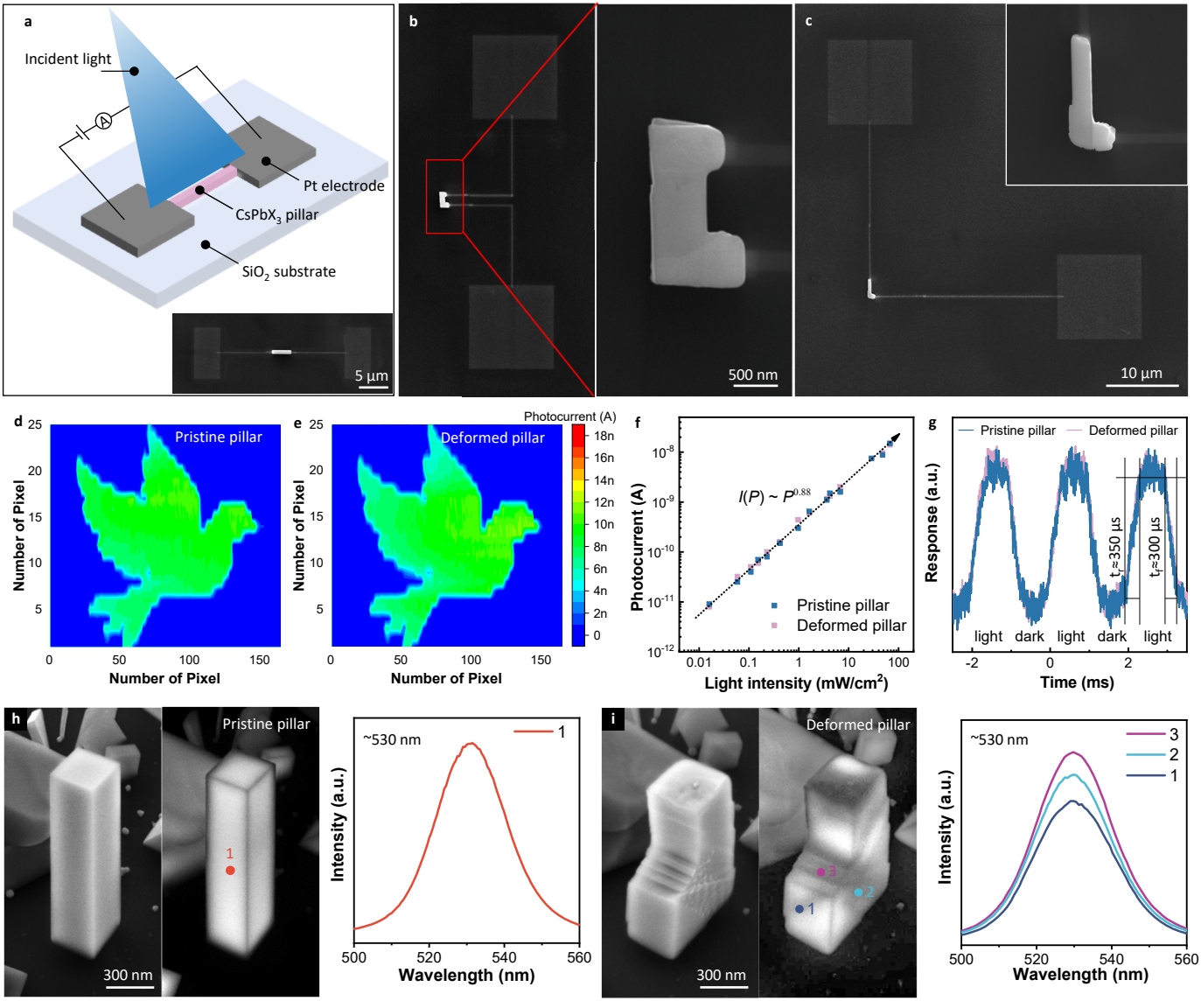
a
Incident light
Pt electrode
CsPbX3 pillar
SiO2 substrate
5 μm
b
500 nm
c
10 μm
d
Pristine pillar
Number of Pixel
Number of Pixel
e
Deformed pillar
Photocurrent (A)
Number of Pixel
Number of Pixel
f
I(P) ~ P0.88
Pristine pillar
Deformed pillar
Photocurrent (A)
Light intensity (mW/cm2)
g
Pristine pillar
Deformed pillar
Response (a.u.)
light
dark
light
dark
light
Time (ms)
h
Pristine pillar
300 nm
~530 nm
Intensity (a.u.)
Wavelength (nm)
i
Deformed pillar
300 nm
~530 nm
Intensity (a.u.)
Wavelength (nm)

Fig. 4